Simultaneous CO_2 Capture and Conversion over Ni-Pd Supported CeO_2 Nanoparticles with Different Morphologies During Catalytic *n*-C_7 Asphaltene Gasification

O.E. Medina, Universidad Nacional de Colombia; D. Galeano-Caro. Universidad Nacional de Colombia; A.F. Pérez-Cadenas, Universidad de Granada; F. Carrasco-Marín, Universidad de Granada; C.A. Franco, Universidad Nacional de Colombia; and F.B. Cortes, Universidad Nacional de Colombia.

Categoría: Marque con una "X"

- Artículo Técnico   [X]
- Tesis Pregrado   [   ]
- Tesis Posgrado   [   ]

Abstract

The main objective of this study is to evaluate multifunctional nanomaterials that allow the capture of CO_2 and its subsequent transformation into valuable sub-products during the catalytic decomposition of asphaltenes in a steam gasification atmosphere for shallow reservoirs. To this aim, three ceria nanoparticles with cubic (C-CeO_2), orthorhombic (O-CeO_2), and spherical (S-CeO_2) were tested in four stages including: *i*) CO_2 capture at 30, 50, 100, and 200 °C between 0.084 and 3.0 MPa, *ii*) dynamic *in-situ* CO_2 capture between 170 and 230 °C at atmospheric pressure, *iii*) dynamic *in-situ* CO_2 capture in the presence of steam between 170 and 230 °C at atmospheric pressure and *iv*) dynamic *in-situ* CO_2 capture in the presence of steam with adsorbed asphaltenes between 170 and 230 °C at atmospheric pressure. CO_2 conversion was analyzed in the last three stages. The best nanoparticle morphology was doped with 1 wt.% of Ni and Pd (C-NiPdCe) and was tested in the same experiments. Dynamic *in-situ* CO_2 capture was estimated by introducing a fixed molar flow (0.296 $mmolCO_2$ min^{-1}) of CO_2 in a TGA device and analyzing the exhaust gases with a mass spectrometer. From the first stage, CO_2 capture increased in the order S-CeO_2 < O-CeO_2 < C-CeO_2 < C-NiPdCe. At 30 °C the CO_2 capture was ~ 7.2, 7.7, 8.0, 9.0 $mmol·g^{-1}$ on S-CeO_2, O-CeO_2, C-CeO_2, and C-NiPdCe, respectively. In addition, the CO_2 capture remains high at all temperatures evaluated. On the other hand, during the second stage during 60 min of isothermal (200 °C) heating without steam, the *in-situ* CO_2 capture was 4.3 mmol, 4.6 mmol, 5.5 mmol, and 5.6 mmol of CO_2 were captured by S-CeO_2, O-CeO_2, C-CeO_2, and C-NiPdCe, respectively. Simmilarly, 0.30 mmol, 0.32 mmol. 0.35 mmol, and 0.38 mmol of CO_2 were converted by the same systems. Then, once steam in injected, the CO_2 capture was reduced. At 200 °C was reduced 3.0%, 2.7%, 2.5%, and 2.0% when the process is assisted by S-CeO_2, O-CeO_2, C-CeO_2, and C-NiPdCe, respectively. In an opposite way, the $\sum X_{i_{exit,t}}$ increased up to 2.85, 2.80, 2.70, and 2.62% in C-NiPdCe, C-CeO_2, O-CeO_2, and S-CeO_2, respectively. Similar trends were found at 170 and 230 °C. During the third stage, the C-CeO_2 nanoparticle capture around 24.3% and converts 15.2%, that is, 3.92 mmol and 2.45 mmol of CO_2 at 200 °C during the 60 min analyzed. Then, the *in-situ* CO_2 capture (%) was reduced in orthorhombic and spherical nanoparticles to 18.6% (3.00 mmol) and 23.7% (3.82 mmol), respectively. Moreover, the C-NiPdCe capture 37%, 34%, and 26%, at 170 °C, 200 °C, and 230 °C of CO_2, respectively, that is, 11.6%, 11.8% and 1.6% more than C-CeO_2 at the same temperatures.

Keywords: Asphaltenes, CO_2 capture, CO_2 conversion, Nanoparticles.

Introduction

The anthropogenic emission of the greenhouse gas CO_2 is considered the main responsible for climate change.[1, 2] In the last century, the concentration of CO_2 in the atmosphere raised from 280 to 400 ppm, increasing the global surface temperature around 0.8°C.[3] It is expected that at the end of this century, the atmospheric CO_2 level will reach 700 ppm, implying an increase in the global surface temperature of up to 5 °C.[3] Therefore, effective measures for controlling CO_2 emissions need to be urgently established. Carbon capture and utilization (CCU) technologies capture CO_2 for further usage,[4-6] which can lead to significantly reductions of greenhouse gas emissions.[7, 8] Nowadays, most studies on CCU technologies focus on evaluating CO_2 capture and utilization in separate steps.[9] However, the large-scale application of technologies to capture and transform CO_2 is limited by the heat transfer required to conduct low-

temperatures for CO_2 capture (<60 °C) and high-temperatures for CO_2 conversion (>500 °C).[10] Hence, implementing multifunctional materials that as sorbent and catalysts appears as an alternative for CO_2 capture and utilization in an integrated process.[11-14] These applications seek the design of reactors where both methods can be carried out.[15, 16] There are different kinf of reactors such as coal-fired power plants,[17] mixed electron and carbonate ion conductor (MECC) membrane,[18] dual- phase membranes,[18] electrochemical reactors,[19] among others.

However, the use of geological petroleum formations where both the capture and conversion of CO_2, as well as the production of other high-quality subproducts has not been proposed yet. Currently, many oilfields use high-temperature technologies (350 °C) that include steam injection under different mechanisms (cyclic, continuous, etc.), mainly focused on the production of heavy and extra-heavy crude oils.[20-23] Steam is injected into a wide range of reservoir depths from 200 ft. In these reservoirs, the pressure reaches up to 3.0 MPa, the reservoir temperature between 40 - 60 °C, and steam injection temperature up to 350 °C.[24-26] Hence, these reservoirs can be suitable for CO_2 capture, storage, and conversion during steam injection processes.[24-30] At these conditions, it is possible to inject gaseous CO_2 with the steam stream. However, the CO_2 capture is limited by diverse geological factors that hinder the storage through conventional mechanisms in terms of adsorption capacity, generally lower than 0.0013 $mmol \cdot g^{-1}$.[31] Hence, a viable option is to promote the CO_2 capture towards adsorption phenomena in shallow reservoirs.[32, 31, 33] Using combined CCUS and steam injection technologies can result in a potential path to increase the volume of crude oil produced, its quality at the same time that CO_2 sequestration and conversion is performed.[34-37]

In this sense, many nanotechnology-based solutions have been proposed to attack, in a separate way, the CO_2 storage in shallow reservoirs,[31, 38, 39] and the enhancement of steam injection processes.[40-44] In the case of geological CO_2 capture, different nanoparticles including carbon,[33] metal oxides,[45] and inorganic nanoparticles,[46] have been employed, obtaining adsorption capacities between 3 and 5 $mmol g^{-1}$ until 3.0 MPa.[33, 38, 47] Previously, our research group developed smart nanomaterials for carbon capture with high selectivity from flue gas streams. As main result, it was obtained an incremental factor of 922 and 730 at 25 and 50 °C, respectively, for the andstone adosprtion capacity using 20 wt.% of nanoparticles.[31, 33]

On the other hand, nanoparticles based on transition element oxides and lanthanides have been proposed to improve steam injection processes,[48-55] mainly through the conversion of crude oil heavy fraction such as asphaltenes into lighter compounds and increase of thermal conductivity of the reservoir. The transformation of asphaltenes means an improvement in crude oil quality since they are the main ones responsible for their high viscosities and low densities.[56, 57] Also, intelligent nanomaterials could result in selective selection asphaltene conversion into H_2 and other high-quality subproducts.[58-60]

However, to our knowledge, there are no studies in specialized literature that report the simultaneous use of nanoparticles for simultaneous CO_2 capture and conversion during the catalytic n-C_7 asphaltene gasification on shallow reservoirs. In this sense, the main objective of this study is to develop a nanoparticle-based technology that allows sequestration of CO_2, with simultaneous conversion of this compound and n-C_7 asphaltenes into high-quality subproducts. For this, three ceria nanoparticles with different morphologies were tested in four stages including: *i*) CO_2 capture at 30, 50, 100, and 200 °C between 0.084 and 3.0 MPa, *ii*) dynamic *in-situ* CO_2 capture between 170 and 230 °C at atmospheric pressure, *iii*) dynamic *in-situ* CO_2 capture in the presence of steam between 170 and 230 °C at atmospheric pressure and i*v*) dynamic *in-situ* CO_2 capture in the presence of steam with adsorbed asphaltenes between 170 and 230 °C at atmospheric pressure. A new landscape is opened with the development of this work to approach thermal enhanced oil recovery methods, capture, and use CO_2, improve the efficiency of the oil and gas industry operations, and reduce greenhouse gas emissions.

Experimental.

Materials. Asphaltenes were isolated from a Colombian extra-heavy crude oil using *n*-heptane purchased by Sigma-Aldrich (St. Louis, MO, USA) with 99% purity following the ASTM standard.[61] Asphaltenes have a C, H, N, S, and O content of 81.7 wt.%, 7.8 wt.%, 0.3 wt.%, 6.6 wt.% 3.6 wt.%, respectively. Asphaltene molecular weight is 645.1 $g \cdot mol^{-1}$. Details of the properties of crude oil and asphaltenes are reported in our previous study.[50] Also, cubic (C-CeO_2), orthorhombic (O-CeO_2), and spherical (S-CeO_2) ceria nanoparticles were used to evaluate asphaltene adsorption/conversion and CO_2 capture/conversion. Doped C-CeO_2 with 1.0 wt.% of Ni and Pd (C-NiPdCe) was considered in this study. Table 1 and 2 summarizes main propertis of the employed nanomaterials. Details of synthesis process, as well as details of the chemical and textural properties of employed nanoparticles are reported in a previous study.[62]

Table 1. Textural properties estimated of synthesized S-CeO_2, C-CeO_2, O-CeO_2, and C-NiPdCe.

Sample	S_{BET} $(m^2 \cdot g^{-1})$	$Wo(CO_2)$	$Lo(CO_2)$	$Wo(N_2)$	$Lo(N_2)$	$V_{0.95}$	$Vmeso_{(BJH)}$
S-CeO_2	22.2	0.17	0.55	0.14	0.75	0.26	0.045
C-CeO_2	32.1	0.22	0.58	0.17	0.79	0.33	0.056
O-CeO_2	28.0	0.21	0.58	0.15	0.78	0.32	0.044
C-NiPdCe	25.5	0.19	0.61	0.15	0.77	0.31	0.053

Asociación Colombiana de Ingenieros de Petróleos – ACIPET
Carrera 14 No. 97-63, Piso 5
PBX: (601) 6411944 - www.acipet.com

Table 2. Chemical properties estimated of synthesized S-CeO$_2$, C-CeO$_2$, O-CeO$_2$, and C-NiPdCe.

Sample	Crystallite size^a (nm)	Lattice Parameter^b (nm) x 10^{-2}	Ce^{3+} (%)	O$_{ads}$ (%)	O$_{latt}$ (%)	Ni^{2+} (NiO) (%)	Pd^{2+} (%)	I$_{(598+1172)}$/I$_{458}$
S-CeO$_2$	12.0	54.09	18.39	41.86	58.14	-	-	0.10
C-CeO$_2$	15.0	54.12	32.60	88.03	11.97	-	-	0.23
O-CeO$_2$	19.0	54.10	26.91	75.94	24.06	-	-	0.19
C-NiPdCe	12.4	54.01	52.4	84.8	15.2	33.5	62.3	0.25

CO$_2$ capture at reservoir conditions. An HP-TGA 750 analyzer (Hullhorst, Germany) was used to evaluate the CO$_2$ capture capacity of CeO$_2$-based nanoparticles at different temperatures including 30 °C, 50 °C, 100 °C, and 200 °C in a range of pressures between 0.084 MPa and 3.0 MPa based on a magnetic levitation technique.[63] The magnetic system provided a monotone electromagnetic field capable of levitating a magnet set on the suspension shaft and sample maintainer. The device was calibrated based on temperature and weight. However, changing the heat conductivity of the gas by pressure and temperature makes temperature calibration at high-pressure conditions very challenging. Therefore, it is essential to measure the Curie temperature in the entire pressure range of the device. The CO$_2$ flow used was 60 mL·min^{-1} in the experiments. The sample mass was adjusted to 30 mg to avoid the impacts of mass/heat transfer and provide enough total surface area for adsorption.[33]

To perform the CO$_2$ adsorption tests, first, a vacuum condition (0.00025 MPa and 120 °C) was used to clean the solid surfaces of the samples for 12 h. Then, pressure, temperature, and gas flow rate were adjusted to the initial conditions. To correct the buoyancy effect of the gas flow, two different runs were made with empty and solid-filled sample containers. Then, the obtained mass profile for each sample was removed for the empty sample container.

Additionally, CO$_2$ capture during several reuses was performed for the best morphology and doped material. For this, the capture of CO$_2$ in the TGA-HP at 3.0 MPa was measured. CO$_2$ desorption was performed by subjecting the sample to a vacuum for 12 hours. After that, a new adsorption cycle is completed. The procedure was repeated 20 times.

The adsorption isotherms were fitted with the Sips model,[64] which considers multilayer adsorption of CO$_2$ over nanoparticles' surfaces. The Sips model is described by Equation 1. Here, b represents the adsorption equilibrium constant, n represents the heterogeneity of the system, N_{ads} (mmol·g^{-1}) and N_m (mmol·g^{-1}) represent the adsorbed amount and maximum adsorption capacity at an equilibrium pressure P (kPa).

$$N_{ads} = N_m \frac{(bP)^{1/n}}{1+(bP)^{1/n}} \tag{1}$$

CO$_2$ capture during asphaltene catalytic gasification. A Asphaltene adsorption over nanoparticles was tested by batch experiments following the protocol described elsewhere and based on a colorimetric method.[57, 65, 66] The nanoparticles containing 0.02 mg·m^{-2} of adsorbed asphaltenes were subjected to *in-situ* CO$_2$ capture. A Q50 thermogravimetric analyzer (TA Instruments, Inc., New Castel, DE, USA) equipped with a mass spectrometer (GC-MS, Shimadzu GC, Japan) was used to study CO$_2$ capture during asphaltene catalytic gasification. These experiments were performed in three main stages. First, CO$_2$ adsorption was calculated in the different nanoparticles by injecting CO$_2$ at 60 mL·min^{-1} (i.e., 0.26926 mmol min^{-1}). Then, CO$_2$ adsorption in the presence of steam was analyzed. In these tests, the H$_2$O$_{(g)}$ flow was fixed at 6.30 mL min^{-1}, and the CO$_2$ flow at 60 mL·min^{-1}. The gasifying atmosphere was simulated using a gas saturator controlled by a thermostatic bath at atmospheric pressure.[67] Finally, nanoparticles containing 0.02 mg·m^{-2} of adsorbed asphaltenes were subjected to similar conditions to determine CO$_2$ capture during asphaltene catalytic gasification. The tests were executed at 170 °C, 200°C, and 230 °C.

CO$_2$ capture was obtained using the equipped TGA device with an online MS spectrometer. The MS was adjusted to measure the moles of CO$_2$ (44.01 g mol^{-1}) at the exit of the TGA. The CO$_2$ capture percentage was obtained using Equation 2, where $CO_{2_{entry,t}}$ and $CO_{2_{exit,t}}$ refer to the moles of CO$_2$ at the entry and exit of the TGA device at a determined time t. Also, the $\sum X_{i_{exit,t}}$ refers to the moles of other gases i produced at a determined time t.

$$CO_2 \ Capture(\%) = \frac{CO_{2_{entry,t}} - (CO_{2_{exit,t}} + \sum X_{i_{exit,t}})}{CO_{2_{entry,t}}} \times 100 \tag{2}$$

Besides, TGA-MS was used to investigate the emitted gases from the catalytic gasification of asphaltenes through a linear ion trap (LIT) mass analyzer with the rate of 0.03 M/Z from 0 to 200 M/Z for determining the gases produced during CO_2 conversion.

Finally, each experiment was repeated three times to ensure the accuracy of the results, obtaining uncertainties of 0.0001 mg and ±0.01 ° C.

Results.

Carbon Capture over CeO₂ nanoparticles

Effect of ceria morphology. Figure 1-panel a shows the experimental adsorption profiles and Sips fits for CO_2 in the materials C-CeO_2, O-CeO_2 and S-CeO_2 at a fixed temperature of 30 °C. According to the IUPAC (International Union of Pure and Applied Chemistry) classification, the adsorption of CO_2 on all materials follows a type Ib isotherm. These isotherms are typical of materials with a high affinity for adsorbate molecules (CO_2) and are characterized by a high slope at pressures below 1.5 MPa. At higher pressures, between 2.5 and 3.0 MPa, a tendency towards stabilization in the amount of CO_2 adsorbed is evident. The shape of the isotherms indicates that the saturation of the active sites of the nanomaterial is reached at these pressure conditions, regardless of the temperature evaluated.[68] The increase in the adsorbed amount by increasing the pressure of the system from 0 to 3 MPa indicates that the adsorption is due to a physical and not a chemical process, for which the nature of the interaction is reversible, and the captured CO_2 can be used later in a desorption/transformation process.[31]

The behavior obtained in the adsorption isotherms is because the CeO_2-based materials have high oxygen vacancies, which promote the physisorption of CO_2 by interactions with the Ce^{3+} present on the surface of the adsorbent.[69, 70] The adsorptive capacity of CO_2 decreases in the direction C-CeO_2 > O-CeO_2 > S-CeO_2 for a fixed pressure. Some chemicals and textural properties could influence the capability of each material to capture CO_2. From Table 1 it is recognized that the micro and mesoporous volume of ceria-nanoparticles follows the order S-CeO_2 < O-CeO_2 < C-CeO_2. Interestingly, other properties like size of mesopore and surface area follows the same order, suggesting that the textural properties of C-CeO_2 are more suitable for CO_2 capture and greater diffusion of CO_2 over the pore space.

Additionally, density functional theory analysis demonstrated that CO_2 is adsorbed on CeO_2 as 3 type of CO_2 adsorbed species including: *i*) monodentate configuration forming carbonate species with two oxygen atoms on its surface, *ii*) bidentate configurations with one oxygen atom on its surface, and *iii*) polydentate carbonate species.[75, 76] The mechanism is favored by the positive surface charges of the ceria that allow interactions between C (from CO_2) and oxygen (from CeO_2). Figure 1.b shows an schematical representation of bidentate and polydentate configurations.[71-73] The bindentate species are considered less stable, whereas monodentate configurations are the most stable with binding energies of -0.31 eV, and preferably formed in (111) crystal facets.[74] In this way, the high capacity of the C-CeO_2 material to capture CO_2 is explained by the presence of highly reactive crystallographic planes such as {111}.[33, 71, 74] Similarly, the lattice parameter (see Table 2) of ceria could improve the adsorption mechanism. Increasing the lattice parameter increases the oxygen vacancies and therefore the vacancies-CO_2 interactions.[75] The tendency is showed in Figure 1.c.
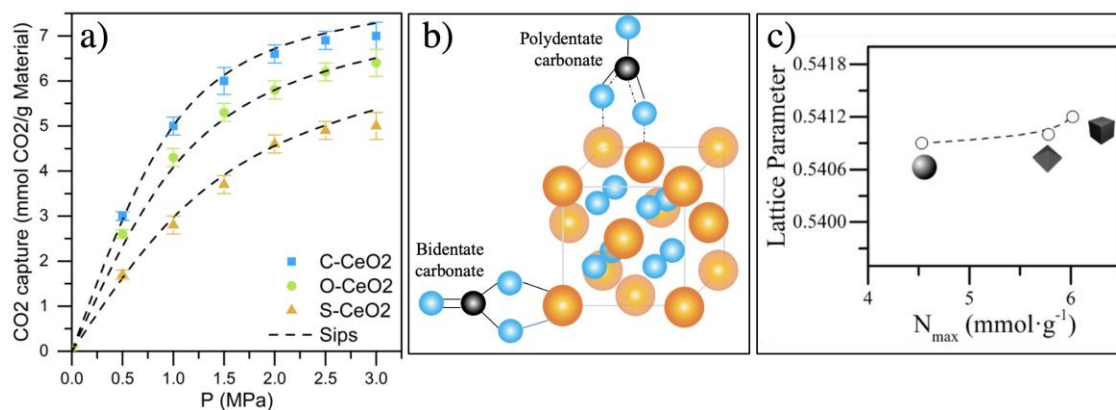

Figure 1. a) High-pressure CO_2 adsorption isotherms for materials C-CeO_2 (blue), O-CeO_2 (green) and S-CeO_2 (orange) at a temperature of 30 °C. The Sips model[64] used for modeling the isotherms is represented as black dotted lines in all cases. b) Interactions CO_2/CeO_2-base materials. Ce, O, and C molecules are represented by orange, blue, and black spheres, respectively. c)

Asociación Colombiana de Ingenieros de Petróleos – ACIPET
Carrera 14 No. 97-63, Piso 5
PBX: (601) 6411944 - www.acipet.com

Relationship between the amount adsorbed and the Lattice parameter for the materials C-CeO$_2$ (cubic), S-CeO$_2$ (orthorhombic) and O-CeO$_2$ (spherical).

Effect of temperature. The effect of temperature on the adsorption of CO_2 in the materials S-CeO$_2$, C-CeO$_2$ and O-CeO$_2$ was evaluated through adsorption isotherms at 30, 50, 100 and 200 °C. The results are shown in Figure 2. It is observed that the amount adsorbed decreases with increasing temperature from 30 to 200 °C due to the highly exothermic nature of the CO_2/CeO$_2$ interactions. At fixed conditions of 1.0 MPa and 30 °C, reductions of 50.0%, 53.5% and 35.7% are observed for C-CeO$_2$, O-CeO$_2$ and S-CeO$_2$, respectively. These results are in agreement with those reported by Ghalandari et al.,[76] and Melouki et al.[77]. The exothermicity of the system provides high energy to the molecules in the vapor phase with increased temperature. Therefore, there will be a lower capacity of adsorption sites to interact with CO_2 particles due to their high diffusion rate.[68]

However, the results suggest that used nanoparticles present a high adsorption capacity at shallow reservoir conditions (T < 100 °C, P < 3.0 MPa), and at steam injection conditions on HO shallow reservoirs (T < 200 °C, P < 3.0 MPa).[33]

Additionally, Melouki et al.[77] also indicate that the adsorption process is reversible, for which the captured CO_2 can be desorbed and subsequently transformed to generate products with higher energetic value.
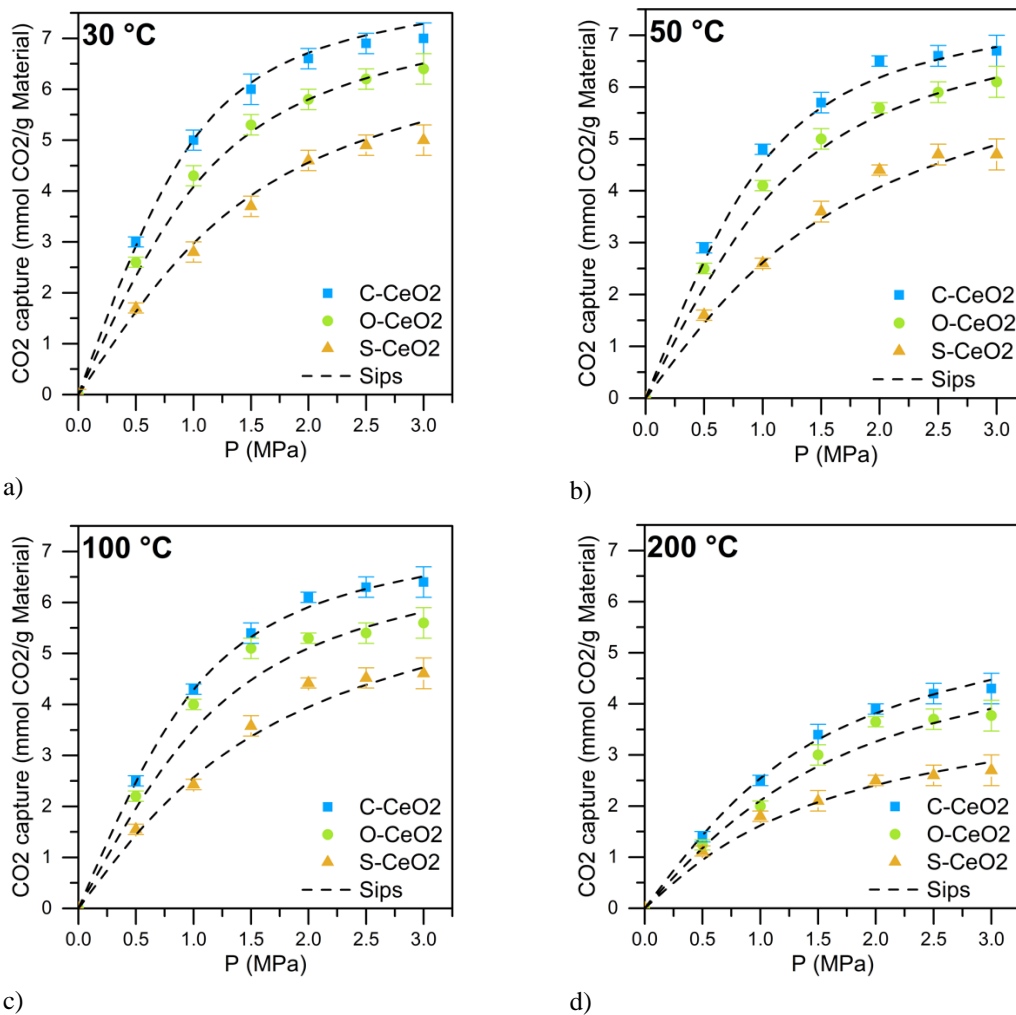

Figure 2. High-pressure CO_2 adsorption isotherms for materials C-CeO$_2$ (blue), O-CeO$_2$ (green) and S-CeO$_2$ (orange) at temperatures of a) 30 °C, b), 50 °C, c) 100 °C and d) 200 °C. The Sips model[64] used for modeling the isotherms is represented as black dotted lines in all cases.

Effect of doped material. The previous results showed that the C-CeO$_2$ material has the highest performance in CO_2 capture under high-pressure and high-temperature conditions. Hence, this material was doped with nickel and palladium as metallic phases under the incipient wet technique mentioned above and was tested under low temperature (30 °C) and high temperature (200 °C) conditions

in the pressure range of 0 and 3.0 MPa. The results obtained are shown in Figure 3. It was observed that the C-CeNiPd material has a much higher adsorptive capacity than the non-doped C-CeO$_2$ material during the CO$_2$ capture process. This trend is because the Ni and Pd metallic phases provide more significant CO$_2$/CeO$_2$ interaction due to Ni^{2+} and Pd^{2+} cations, which facilitate the formation of oxygen vacancies between the surface and the mass of the base material.[78]

Interestingly, it was found a relationship between the maximum adsorptive capacity with I$_{(598+1172)}$/I$_{458}$ and the percentage of Ce^{3+}. The increment in both properties (regardless non-doped nanoparticles) improved the adsorption capacity of the nanoparticle. Different defects including O^{2-} are induced by ceria, nickel, and palladium cations, increasing the values of I$_{(598+1172)}$/I$_{458}$ and therefore, increasing the proportion of Ce^{3+}.

On ther other hand, similarly to the non-doped ceria nanoparticles, a reduction of the adsorptive capacity is observed with increasing temperature. At a fixed pressure (3.0 MPa) there is a reduction of 35% of the CO$_2$ captured when temperature increased from 30 to 200 °C.
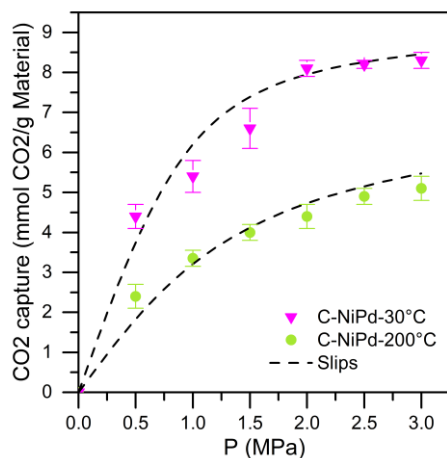

Figure 3. a) High-pressure CO$_2$ adsorption isotherms on C-CeNiPd at 30 °C and 200 °C. The Sips model used for modeling the isotherms is represented as black dotted lines in all cases.

In-situ CO$_2$ Capture during n-C$_7$ Asphaltene Gasification over CeO$_2$ – based Nanoparticles. During TGA tests are analyzed two important variables. The CO$_2$ capture which refers to the moles of CO$_2$ adsorbed on the nanoparticles and depends of the moles of CO$_2$ at the entry and exit of the TGA device at a determined time t and the CO$_2$ conversion which was defined as the $\sum X_{i_{exit,t}}$, that is, the moles of other gases i produced at a determined time t. Both variables were obtained by the TGA-MS configuration.

In-situ CO$_2$ capture with and without steam. *In-situ* CO$_2$ capture was initially measured over CeO$_2$ and NiPd-doped CeO$_2$ nanoparticles without asphaltenes in the presence and absence of steam to verify the dynamic CO$_2$ adsorption at 170, 200, and 230 °C and atmospheric pressure. The results at 200 °C are shown in Figure 5 whereas the results at 170 and 230 °C are shown in Figure 2 of Appendix A. From panel a it is observed that during 60 min of isothermal heating without steam, the *in-situ* CO$_2$ capture (%) at 200 °C was 27.0%, 28.7%, 34.5%, and 35% for S-CeO$_2$, O-CeO$_2$, C-CeO$_2$, and C-NiPdCe, respectively. Regarding these results, the capture % at 170 °C was slightly higher and the opposite occurs at 230 °C. This result agrees well with the reported in section 3.1. Analyzing the CO$_2$ conversion (%vol of $\sum X_{i_{exit,t}}$), it followed a similar behavior than the captured CO$_2$. The %vol of $\sum X_{i_{exit,t}}$ for S-CeO$_2$, O-CeO$_2$, C-CeO$_2$, and C-NiPdCe was 1.9%, 2.0%, 2.2%, and 2.4%, respectively. Considering the molar flow of CO$_2$ (0.296 mmol·min^{-1}), during 60 min, around 16.15 mmol of CO$_2$ were injected. It means that at 200 °C, 4.3 mmol, 4.6 mmol, 5.5 mmol, and 5.6 mmol of CO$_2$ were captured by S-CeO$_2$, O-CeO$_2$, C-CeO$_2$, and C-NiPdCe, respectively. Simmilarly, 0.30 mmol, 0.32 mmol. 0.35 mmol, and 0.38 mmol of CO$_2$ were converted by the same systems.

Based on these results, the C-NiPdCe is the material with the highest CO$_2$ capture and conversion. Between the supports with different morphologies, both variables increase in the trend: S-CeO$_2$ < O-CeO$_2$ < C-CeO$_2$.

Then, once steam in injected (Panels b), the CO$_2$ capture was reduced. Analyzing the results at 200 °C, it was reduced 3.0%, 2.7%, 2.5%, and 2.0% when the process is assisted by S-CeO$_2$, O-CeO$_2$, C-CeO$_2$, and C-NiPdCe, respectively. In an opposite way, the $\sum X_{i_{exit,t}}$ increased up to 2.85, 2.80, 2.70, and 2.62% in C-NiPdCe, C-CeO$_2$, O-CeO$_2$, and S-CeO$_2$, respectively. Similar trends were found at 170 and 230 °C. The increment in CO2 conversion under steam presence could be a result of the interactions between

Asociación Colombiana de Ingeníeros de Petróleos – ACIPET
Carrera 14 No. 97-63, Piso 5
PBX: (601) 6411944 - www.acipet.com

both molecules and the nanoparticles. It is reported that adsorption of CO_2 is strongly affected by the overwhelming competitive adsorption of steam on CO_2 adsorbents which can react at high temperatures.[82]

Under these conditions, it is confirmed that the nanoparticles can capture CO_2 in the presence and absence of steam molecules.
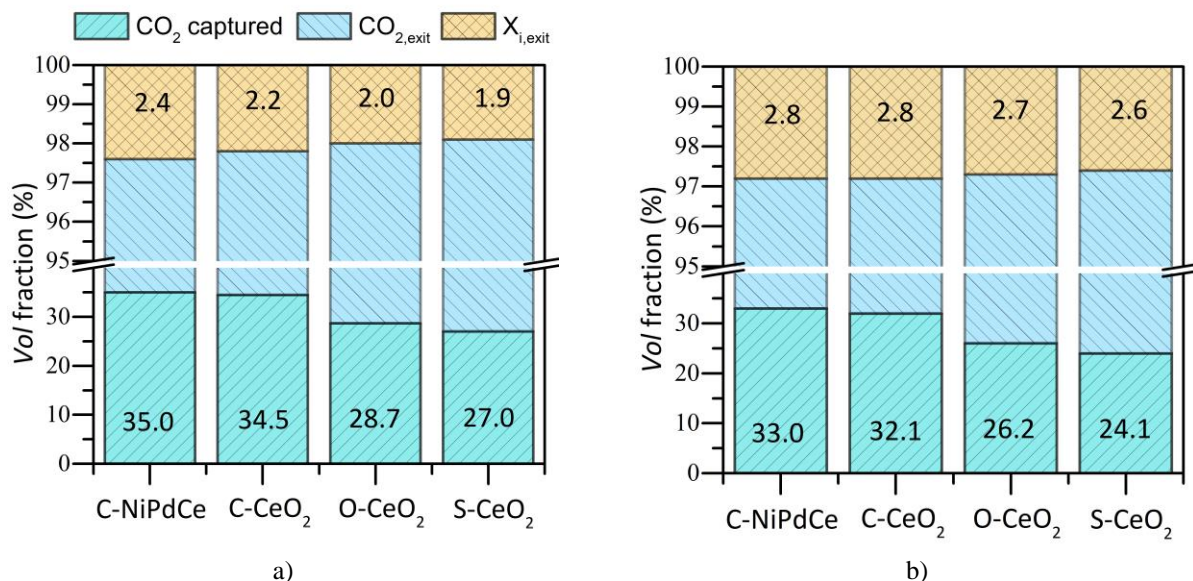

Figure 5. Volume fraction (%) of *in-situ* CO_2 captured, CO_2 at the exit of TGA device, and CO_2 conversion ($\sum X_{i_{exit,t}}$) in CeO_2 and doped CeO_2 nanoparticles a) without and b) with steam at 200 °C.

Effect of ceria morphology on in-situ CO_2 Capture during n-C_7 Asphaltene Gasification. This section focuses on evaluating CO_2 capture based on a scenario of CO_2 injection into a steam stream, in which CO_2 will contact the asphaltene-containing nanocatalyst where CO_2 capture, and conversion is expected to occur. During this process, nanocatalyss also converts the adsorbed asphaltenes, generating different types of by-products through different reactions that can be assisted by the captured CO_2.

Figure 6 shows the results of *in-situ* CO_2 capture in asphaltenes-containing C-CeO_2 at 200 °C and atmospheric pressure. With increasing time, the CO_2 captured % increased because of the increment in asphaltene conversion. The asphaltene conversion on the different nanoparticle is shown in Figure 2 of the Appendix A. Once the asphaltenes are transformed, the availability of active sites for CO_2 anchoring increases. The results suggest that asphaltenes block CO_2-CeO_2 interactions. Because ceria is a Lewis base, it is thermodynamically desirable for asphaltene and CO_2 adsorption. However, the adsorbed asphaltenes limit CO_2-CeO_2 interactions because they are insoluble in CO_2, and the asphaltene-CO_2 interactions are not expected.[83]

Similarly, CO_2 conversion ($\sum X_{i_{exit,t}}$) is time dependent and increases with increasing asphaltene conversion (increasing time).

Based on the assumption that the activation of the C=O bond of CO_2 molecule needs to introduce a reductant carrying H and/or C atoms, such as H_2 (from steam) and hydrocarbons (like asphaltenes),[84-86] nanomaterials are expected to take advantage of both sources to achieve a correct conversion of CO_2. At 60 min, 16.15 mmol of CO_2 were injected into the TGA device. The C-CeO_2 nanoparticle capture around 24.3% and converts 15.2%, that is, 3.92 mmol and 2.45 mmol of CO_2 are captured and converted at 200 °C during the 60 min analyzed.
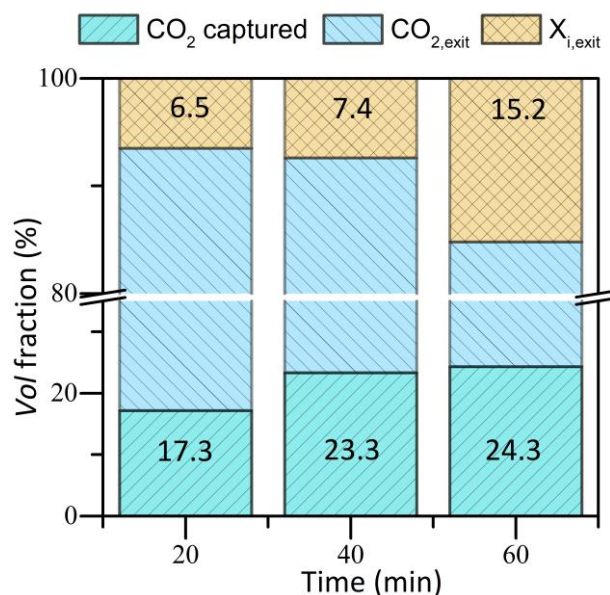
Figure 6. Volume fraction (%) of *in-situ* CO_2 captured, CO_2 at the exit of TGA device, and CO_2 conversion ($\sum X_{i_{exit,t}}$) during *n*-C_7 asphaltene catalytic gasification using C-CeO$_2$ at 200 °C.

To analyze the effect of ceria morphology on *in-situ* CO_2 capture, a fixed temperature of 200 °C was selected and results for orthorhombic and spherical nanoparticles are shown in Figure 7. Based on the information of Figures 6 and 7, CO_2 capture during asphaltene consumption follows the increasing order: S-CeO$_2$ < O-CeO$_2$ < C-CeO$_2$. According to the conversion results (Figure 2 of the Appendix A), the spherical nanoparticles have a large part of the active sites occupied by asphaltene molecules during the analyzed time (lower conversion degree), which are progressively decomposed into light hydrocarbons and gaseous products that are desorbed from the catalyst surface, leaving active sites available to interact with CO_2. In this sense, the greatest capture of CO_2 occurs when most of the asphaltene has been converted and desorbed from the catalyst surface.

In-situ CO_2 capture (%) was 18.6% (3.00 mmol), 23.7% (3.82 mmol), and 24.3% (3.92 mmol) in S-CeO$_2$, O-CeO$_2$, and C-CeO$_2$, respectively, at 60 min of isothermal heating at 200 °C. The change in the morphology of the CeO$_2$ systems presented different yields in the *in-situ* CO_2 uptake because of their different chemical and textural properties. According to the literature, the exposure of the more reactive (100), (100), and (111) crystal facets facilitate the formation of oxygen vacancies on the ceria surface. We verified that cubic nanoparticle exposes more reactive facets than orthorhombic and spherical nanoparticles.[62] Hence, it is speculated that the surface defects on the CeO$_2$ contributed to the oxygen storage capacity and consequently in the *in-situ* CO_2 capture. Liu and co-workers report similar results.[87] Also, Li and co-workers[88] found that CO_2 adsorption is performed in bidentate carbonate and bridge carbonate over (111) planes exhibited in C-CeO$_2$. These systems are characterized for the stability of the bridge carbonate on the catalyst's surface.

In addition, CeO$_2$ with abundantly exposed oxygen vacancies is a potent surface for gas adsorption,[87] and therefore, cubic nanoparticles have advantages over others because the formation of oxygen vacancies in the high energy facets enhances the OSC capacity.[89] The $I_{(598+1172)}/I_{458}$ ratio increases in the order S-CeO$_2$ (0.10) < O-CeO$_2$ (0.19) < C-CeO$_2$ (0.23).

In the same way, Ce^{3+} ions concentration enhances the CO_2 capture. This property goes hand in hand with oxygen vacancies. The formation of an oxygen vacancy requires the formation of two Ce^{3+} by the reduction of Ce^{4+}.[88] During the reduction of Ce^{4+}, a small polaron is formed by the distortion of the surrounding oxygen shell to screen the charge when the Ce_{4f} state is occupied. Both properties (oxygen vacancies position and ceria polarons) influence the energy required for the formation of crystalline defects, and this in turn has a critical impact on interactions with CO_2.[90] In this way, CO_2 molecules easily interact with Ce^{3+} arranged on the CeO$_2$ surface. As the cubic nanoparticle has a higher content of Ce^{3+} (48.81%) than orthorhombic (44.3%) and spherical (42.56%), the capture increases. Likewise, the conversion of asphaltenes is greater at shorter times in the same system, and therefore many active sites are vacated faster for *in-situ* CO_2 adsorption.

Regardless the CO_2 conversion ($\sum X_{i_{exit,t}}$), it increased in the order S-CeO$_2$ < O-CeO$_2$ < C-CeO$_2$. Around 15.2% (2.45 mmol),

14.7% (2.37 mmol), and 12.2% (1.97 mmol) of the CO_2 was converted by C-CeO$_2$, O-CeO$_2$, and S-CeO$_2$, respectively. It is corroborated that, the capacity of the materials to convert CO_2 is influenced by the morphology which in turn modify the oxygen storage capacity, textural properties, redox cycling, and therefore its participation as a three-way catalyst in many chemical

Asociación Colombiana de Ingenieros de Petróleos – ACIPET
Carrera 14 No. 97-63, Piso 5
PBX: (601) 6411944 - www.acipet.com

reactions.[91-93] In this case, the cubic nanoparticle presents the best yield in CO_2 conversion as a result of the higher Ce^{3+} exposure on its surface,[87, 94] In addition, cubic material showed the highest performance in asphaltene conversion (Figure 2 of Appendix A).
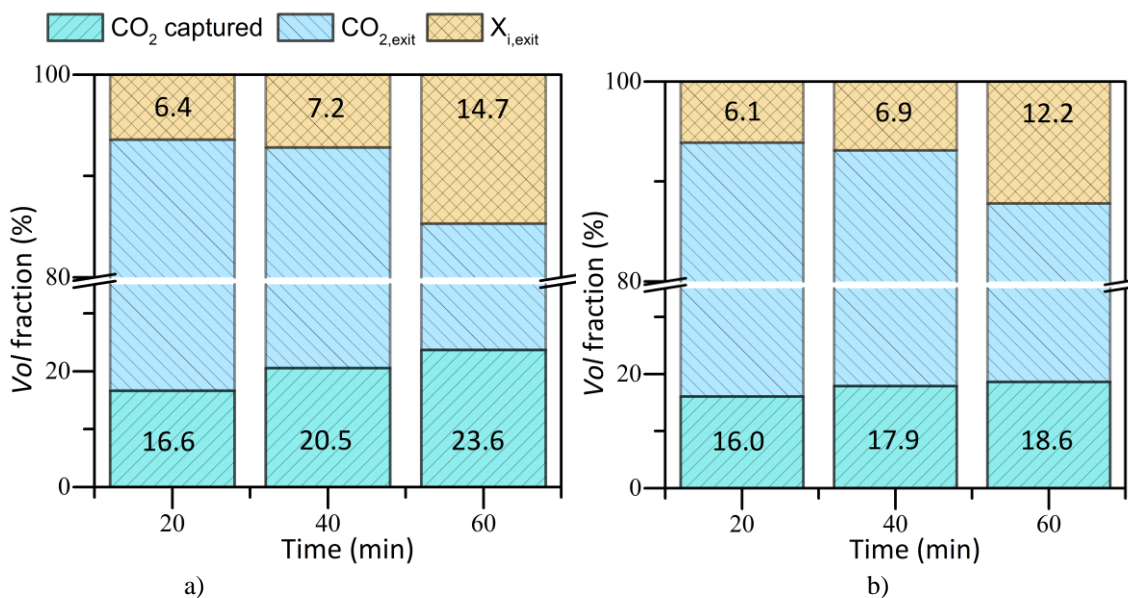

Figure 7. Volume fraction (%) of *in-situ* CO_2 captured, CO_2 at the exit of TGA device, and CO_2 conversion ($\sum X_{i_{exit,t}}$) during *n*-C_7 asphaltene catalytic gasification using a)O-CeO_2 and b)S-CeO_2 at 200 °C.

Effect of doped material. Figure 8 shows the volume fraction (%) of *in-situ* CO_2 captured, CO_2 at the exit of TGA device, and and CO_2 conversion ($\sum X_{i_{exit,t}}$) during *n*-C_7 asphaltene catalytic gasification for doped cubic ceria nanoparticles (C-NiPdCe) as a function of time at different temperatures (170, 200, and 230 °C). The *in-situ* capture of CO_2 and %*vol* of $\sum X_{i_{exit,t}}$ on the doped material follow a similar behavior to non-doped systems. At the end of the analyzed time (60 min), the CO_2 capture (%) was close to 37%, 34%, and 26%, at 170 °C, 200 °C, and 230 °C, respectively, that is, 11.6%, 11.8% and 1.6% more than C-CeO_2 at the same temperatures. Similarly, for a fixed temperature (200 °C) and 60 min, the C-NiPdCe capture 15.4% (2.48 mmol) and 17.3% (2.79 mmol) more than O- CeO_2 and S-CeO_2, respectively.

The highest yield for the doped material is related to an increase in Ce^{3+} phases (52.4%). This stoichiometric phase generally occurs in small oxygen-deficient nanoparticles concentrated in low-coordination Ce, so the concentration of Ce^{3+} is proportional to the dispersion of NiO and PdO. Also, the oxygen vacancies content increases in the CeO_2 lattice ($I_{(598+1172)}/I_{458}$ ratio = 0.25) after Ni and Pd entered the lattice due to the reduction of the Ce crystallite size (C-NiPdCe: 12.4 nm, C-CeO_2: 15 nm). This result is further evidenced by the increase in the lattice oxygen by adding Ni and Pd (C-NiPdCe: 15.2% and C-CeO_2: 11.9%). It has been noted that the high-mobility lattice oxygen on CeO_2 is highly active to bond with CO_2.

On the other hand, the % *vol* of $\sum X_{i_{exit,t}}$ during the analyzed time (60 min) at 170 °C, 200 °C, and 230°C was 14.3 (2.30 mmol), 16.9 (2.72 mmol), and 17.2% (2.77 mmol), respectively. Regarding non-doped materials, the C-NiPdCe present a higher percentage of CO_2 converted at all temperatures because of the catalytic activity of the active phases of Ni and Pd and the Support-Metal Strong Interactions (SMSI). Compared with C-CeO_2 (support with the highest efficiency in *in-situ* CO_2 capture), the C-NiPdCe shows a higher overall CO_2 uptake. Indeed, the Ni and Pd phases promoted the CO_2 affinity of CeO_2, thereby accelerating the CO_2 diffusion rate, which is confirmed by the higher capture at lower times on the CeO_2-modified system.

All these reveal that adding Ni and Pd would enhance the CO_2 affinity of CeO_2 during asphaltene catalytic steam gasification. These results underline the importance of CeO_2 modification to bifunctional material for successful implementation of the isothermal asphaltene steam gasification and CO_2 capture.
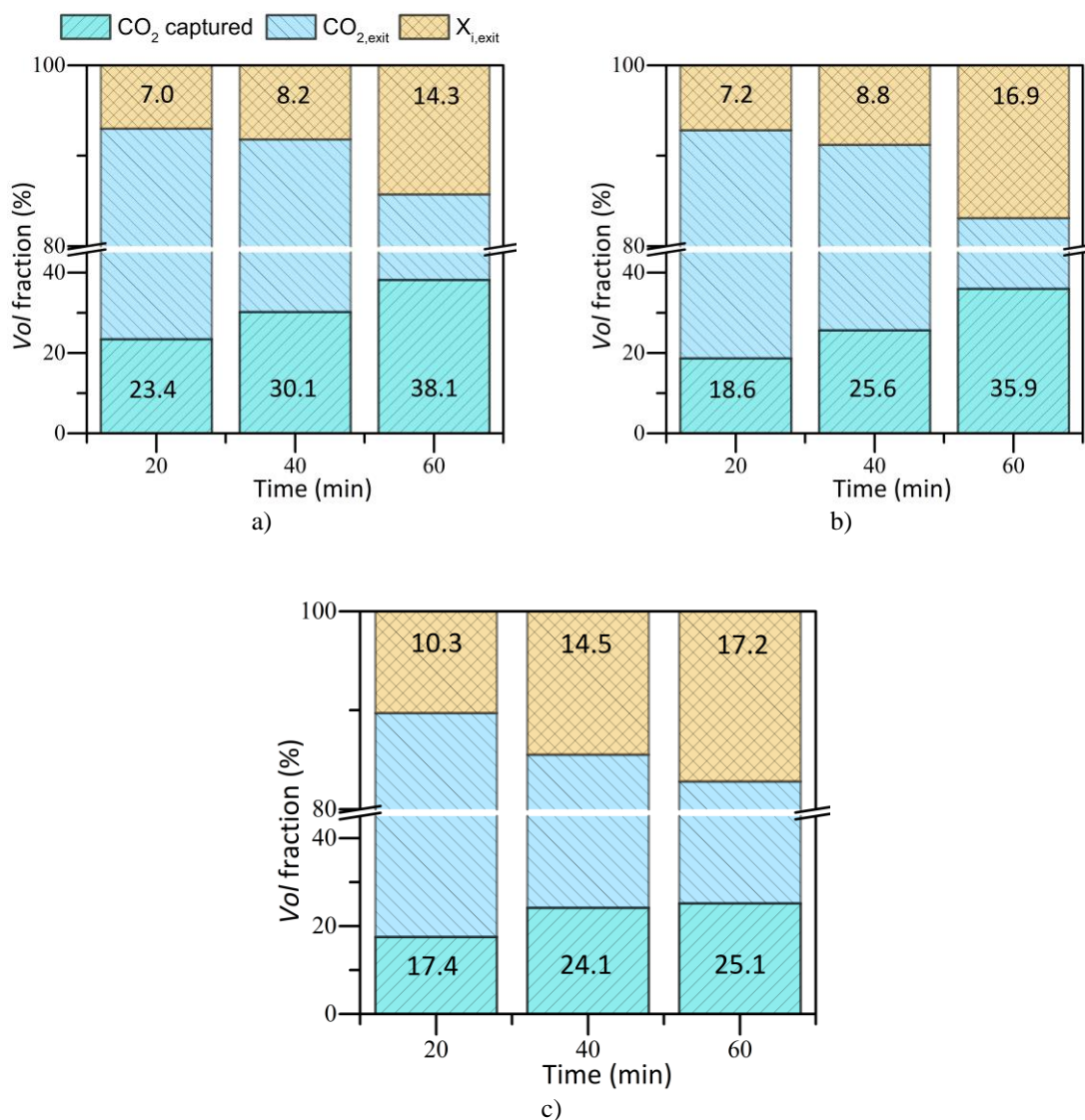
Figure 8. Volume fraction (%) of *in-situ* CO_2 captured, CO_2 at the exit of TGA device, and CO_2 conversion ($\sum X_{i_{exit,t}}$) during *n*-C_7 asphaltene catalytic gasification using C-NiPdCe at a) 170 °C, b) 200 °C, and c) 230°C.

Conclusions.

Three ceria nanoparticles with cubic (C-CeO_2), orthorhombic (O-CeO_2), and spherical (S-CeO_2) were tested in CO_2 capture and conversion during *n*-C_7 asphaltene steam gasification. The best nanoparticle was doped with 1 wt.% in mass fraction of Ni and Pd (C-NiPdCe). First, asphaltene conversion was evaluated in all systems obtaining 100% conversion for all samples at 170 °C, 200 °C, and 230°C. The time required to obtain 100% conversion increased in the trend: C-NiPdCe < C-CeO_2 < O-CeO_2 < S-CeO_2. During the second experiment, CO_2 uptake was tested at different pressures. The adsorptive capacity of CO_2 increased in the direction S-CeO_2 < O-CeO_2 < C-CeO_2 < C-CeNiPd. The functionalization with the metallic phases significantly increases the adsorptive capacity of ceria support, obtaining a high CO_2 capture capacity during the 20 adsorption/desorption cycles, suggesting the high thermal stability of the materials. Then, CO_2 capture was evaluated during *n*-C_7 asphaltene decomposition. The results reveal that *in-situ* CO_2 capture (%) was 19.5%, 23.3%, and 26.2% in S-CeO_2, O-CeO_2, and C-CeO_2, respectively, at 60 minutes of isothermal heating at 170 °C. The capture rate decreased with temperature and reached the minimum at 230 °C. Interestingly, oxygen vacancies concentration and Ce^{3+} content was found to follow the same trend that *in-situ* CO_2 capture. This result suggests that both properties enhance the interactions between CO_2 and CeO_2. Moreover, the C-NiPdCe presents 38.1% of in-situ CO_2 capture at 170 °C, due to this system having a higher content of

Asociación Colombiana de Ingenieros de Petróleos – ACIPET
Carrera 14 No. 97-63, Piso 5
PBX: (601) 6411944 - www.acipet.com

oxygen vacancies and Ce^{3+} phases. The presence of Ni and Pd also increases the interactions with CO_2 due to the increase in Lewis basic sites on the catalyst.

References

1.   Medina, O. E.; Olmos, C.; Lopera, S. H.; Cortés, F. B.; Franco, C. A., Nanotechnology applied to thermal enhanced oil recovery processes: a review. *Energies* **2019,** 12, (24), 4671.
2.   Dabbous, M. K.; Fulton, P. F., Low-temperature-oxidation reaction kinetics and effects on the in-situ combustion process. *Society of Petroleum Engineers Journal* **1974,** 14, (03), 253-262.
3.   Kök, M. V.; Karacan, Ö.; Pamir, R., Kinetic analysis of oxidation behavior of crude oil SARA constituents. *Energy & Fuels* **1998,** 12, (3), 580-588.
4.   Acevedo, S.; Castillo, J.; Vargas, V.; Castro, A.; Delgado, O. Z.; Ariza, C. A. F.; Cotés, F. B.; Bouyssiere, B., Suppression of Phase Separation as a Hypothesis to Account for Nuclei or Nanoaggregate Formation by Asphaltenes in Toluene. *Energy & Fuels* **2018**.
5.   Liu, D.; Hou, J.; Luan, H.; Pan, J.; Song, Q.; Zheng, R., Coke yield prediction model for pyrolysis and oxidation processes of low-asphaltene heavy oil. *Energy & Fuels* **2019,** 33, (7), 6205-6214.
6.   Amrollahi Biyouki, A.; Hosseinpour, N.; Nassar, N. N., Pyrolysis and Oxidation of Asphaltene-Born Coke-like Residue Formed onto in Situ Prepared NiO Nanoparticles toward Advanced in Situ Combustion Enhanced Oil Recovery Processes. *Energy & fuels* **2018,** 32, (4), 5033-5044.
7.   Zhao, S.; Pu, W.; Yuan, C.; Peng, X.; Zhang, J.; Wang, L.; Emelianov, D. A., Thermal behavior and kinetic triplets of heavy crude oil and its SARA fractions during combustion by high-pressure differential scanning calorimetry. *Energy & fuels* **2019,** 33, (4), 3176-3186.
8.   Yuan, C.; Varfolomeev, M. A.; Emelianov, D. A.; Eskin, A. A.; Nagrimanov, R. N.; Kok, M. V.; Afanasiev, I. S.; Fedorchenko, G. D.; Kopylova, E. V., Oxidation behavior of light crude oil and its SARA fractions characterized by TG and DSC techniques: differences and connections. *Energy & fuels* **2018,** 32, (1), 801-808.
9.   Medina, O. E.; Gallego, J.; Rodríguez, E.; Franco, C. A.; Cortés, F. B., Effect of pressure on the oxidation kinetics of Asphaltenes. *Energy & Fuels* **2019,** 33, (11), 10734-10744.
10.   Medina, O. E.; Gallego, J.; Nassar, N. N.; Acevedo, S. A.; Cortés, F. B.; Franco, C. A., Thermo-Oxidative Decomposition Behaviors of Different Sources of n-C7 Asphaltenes at High-Pressure Conditions. *Energy & Fuels* **2020**.
11.   Moncayo-Riascos, I.; Taborda, E.; Hoyos, B. A.; Franco, C. A.; Cortés, F. B., Theoretical-experimental evaluation of rheological behavior of asphaltene solutions in toluene and p-xylene: Effect of the additional methyl group. *Journal of Molecular Liquids* **2020,** 303, 112664.
12.   Tanaka, R.; Hunt, J. E.; Winans, R. E.; Thiyagarajan, P.; Sato, S.; Takanohashi, T., Aggregates structure analysis of petroleum asphaltenes with small-angle neutron scattering. *Energy & fuels* **2003,** 17, (1), 127-134.
13.   Lee, H.; Lee, Y.-K., Effects of the asphaltene structure and the tetralin/heptane solvent ratio on the size and shape of asphaltene aggregates. *Physical Chemistry Chemical Physics* **2017,** 19, (21), 13931-13940.
14.   Larichev, Y. V.; Nartova, A.; Martyanov, O., The influence of different organic solvents on the size and shape of asphaltene aggregates studied via small-angle X-ray scattering and scanning tunneling microscopy. *Adsorption Science & Technology* **2016,** 34, (2-3), 244-257.
15.   Hu, D.; Gu, X.; Cui, B.; Pei, J.; Zhang, Q., Modeling the oxidative aging kinetics and pathways of asphalt: A ReaxFF molecular dynamics study. *Energy & Fuels* **2020,** 34, (3), 3601-3613.
16.   Lan, T.; Zeng, H.; Tang, T., Understanding adsorption of violanthrone-79 as a model asphaltene compound on quartz surface using molecular dynamics simulations. *The Journal of Physical Chemistry C* **2018,** 122, (50), 28787-28796.
17.   Law, J. C.; Headen, T. F.; Jiménez-Serratos, G.; Boek, E. S.; Murgich, J.; Müller, E. A., Catalogue of Plausible Molecular Models for the Molecular Dynamics of Asphaltenes and Resins Obtained from Quantitative Molecular Representation. *Energy & Fuels* **2019,** 33, (10), 9779-9795.
18.   Hosseini-Dastgerdi, Z.; Tabatabaei-Nejad, S.; Khodapanah, E.; Sahraei, E., A comprehensive study on mechanism of formation and techniques to diagnose asphaltene structure; molecular and aggregates: a review. *Asia-Pacific Journal of Chemical Engineering* **2015,** 10, (1), 1-14.
19.   Barre, L.; Espinat, D.; Rosenberg, E.; Scarsella, M., Colloidal structure of heavy crudes and asphaltene solutions. *Revue de l'Institut Français du Pétrole* **1997,** 52, (2), 161-175.
20.   Medina, O. E.; Gallego, J.; Acevedo, S.; Riazi, M.; Ocampo-Pérez, R.; Cortés, F. B.; Franco, C. A., Catalytic Conversion of n-C7 Asphaltenes and Resins II into Hydrogen Using CeO2-Based Nanocatalysts. *Nanomaterials* **2021,** 11, (5), 1301.
21.   Tanaka, R.; Sato, E.; Hunt, J. E.; Winans, R. E.; Sato, S.; Takanohashi, T., Characterization of asphaltene aggregates using X-ray diffraction and small-angle X-ray scattering. *Energy & fuels* **2004,** 18, (4), 1118-1125.

22. Eyssautier, J.; Frot, D.; Barré, L., Structure and dynamic properties of colloidal asphaltene aggregates. *Langmuir* **2012,** 28, (33), 11997-12004.

23. Larichev, Y. V.; Martyanov, O., The dynamics of asphaltene aggregates in heavy crude oils on a nanometer scale studied via small-angle X-ray scattering in situ. *Journal of Petroleum Science and Engineering* **2018,** 165, 575-580.

24. Petoukhov, M. V.; Franke, D.; Shkumatov, A. V.; Tria, G.; Kikhney, A. G.; Gajda, M.; Gorba, C.; Mertens, H. D.; Konarev, P. V.; Svergun, D. I., New developments in the ATSAS program package for small-angle scattering data analysis. *Journal of applied crystallography* **2012,** 45, (2), 342-350.

25. Gimzewski, E., An accurate and compact high-pressure thermogravimetric analyser. *Journal of thermal analysis* **1991,** 37, (6), 1251-1260.

26. Medina, O. E.; Gallego, J.; Rodriguez, E.; Franco, C. A.; Cortés, F. B., Effect of Pressure on the Oxidation Kinetics of Asphaltenes. *Energy & Fuels* **2019**.

27. Xu, Z.; Wang, Y.; Cao, J.; Chai, J.; Cao, C.; Si, Z.; Li, Y., Adhesion between asphalt molecules and acid aggregates under extreme temperature: A ReaxFF reactive molecular dynamics study. *Construction and Building Materials* **2021,** 285, 122882.

28. Headen, T.; Boek, E.; Jackson, G.; Totton, T.; Müller, E., Simulation of asphaltene aggregation through molecular dynamics: Insights and limitations. *Energy & Fuels* **2017,** 31, (2), 1108-1125.

29. Jorgensen, W.; Maxwell, D.; Tirado-Rives, J., Optimized potential for liquid simulations. *J. Am. Chem. Soc* **1996,** 118, 11225-11236.

30. Jorgensen, W. L.; Maxwell, D. S.; Tirado-Rives, J., Development and testing of the OPLS all-atom force field on conformational energetics and properties of organic liquids. *Journal of the American Chemical Society* **1996,** 118, (45), 11225-11236.

31. Watkins, E. K.; Jorgensen, W. L., Perfluoroalkanes: Conformational analysis and liquid-state properties from ab initio and Monte Carlo calculations. *The Journal of Physical Chemistry A* **2001,** 105, (16), 4118-4125.

32. Plimpton, S., Fast parallel algorithms for short-range molecular dynamics. *Journal of computational physics* **1995,** 117, (1), 1-19.

33. Humphrey, W.; Dalke, A.; Schulten, K., VMD: visual molecular dynamics. *Journal of molecular graphics* **1996,** 14, (1), 33-38.

34. Senneca, O.; Vorobiev, N.; Wütscher, A.; Cerciello, F.; Heuer, S.; Wedler, C.; Span, R.; Schiemann, M.; Muhler, M.; Scherer, V., Assessment of combustion rates of coal chars for oxy-combustion applications. *Fuel* **2019,** 238, 173-185.

35. Niksa, S.; Liu, G.-S.; Hurt, R. H., Coal conversion submodels for design applications at elevated pressures. Part I. devolatilization and char oxidation. *Progress in Energy and Combustion Science* **2003,** 29, (5), 425-477.

36. Liu, G.-S.; Niksa, S., Coal conversion submodels for design applications at elevated pressures. Part II. Char gasification. *Progress in energy and combustion science* **2004,** 30, (6), 679-717.

37. Yen, T. F.; Erdman, J. G.; Pollack, S. S., Investigation of the structure of petroleum asphaltenes by X-ray diffraction. *Analytical chemistry* **1961,** 33, (11), 1587-1594.

38. AlHumaidan, F. S.; Hauser, A.; Rana, M. S.; Lababidi, H. M., NMR Characterization of Asphaltene Derived from Residual Oils and Their Thermal Decomposition. *Energy & Fuels* **2017,** 31, (4), 3812-3820.

39. Vukovic, J. P.; Novak, P.; Jednacak, T., NMR Spectroscopy as a Tool for Studying Asphaltene Composition. *Croatica Chemica Acta* **2019,** 92, (3), 1G-1G.

40. Retcofsky, H.; Schweighardt, F.; Hough, M., Determination of aromaticities of coal derivatives by nuclear magnetic resonance spectrometry and the Brown-Ladner equation. *Analytical Chemistry* **1977,** 49, (4), 585-588.

41. Pierre, C.; Barré, L.; Pina, A.; Moan, M., Composition and heavy oil rheology. *Oil & Gas Science and Technology* **2004,** 59, (5), 489-501.

42. Taborda, E. A.; Alvarado, V.; Franco, C. A.; Cortés, F. B., Rheological demonstration of alteration in the heavy crude oil fluid structure upon addition of nanoparticles. *Fuel* **2017,** 189, 322-333.

43. Ramírez, L.; Moncayo-Riascos, I.; Cortés, F. B.; Franco, C. A.; Ribadeneira, R., Molecular Dynamics Study of the Aggregation Behavior of Polycyclic Aromatic Hydrocarbon Molecules in n-Heptane–Toluene Mixtures: Assessing the Heteroatom Content Effect. *Energy & Fuels* **2021,** 35, (4), 3119-3129.

44. Moncayo-Riascos, I.; Taborda, E.; Hoyos, B. A.; Franco, C. A.; Cortés, F. B., Effect of resin/asphaltene ratio on the rheological behavior of asphaltene solutions in a de-asphalted oil and p-xylene: A theoretical–experimental approach. *Journal of Molecular Liquids* **2020,** 315, 113754.

45. Johansson, B.; Friman, R.; Hakanpää-Laitinen, H.; Rosenholm, J. B., Solubility and interaction parameters as references for solution properties II: Precipitation and aggregation of asphaltene in organic solvents. *Advances in colloid and interface science* **2009,** 147, 132-143.

46. Pal, R., A new model for the viscosity of asphaltene solutions. *The Canadian Journal of Chemical Engineering* **2015,** 93, (4), 747-755.

47. Kuakpetoon, D.; Wang, Y.-J., Structural characteristics and physicochemical properties of oxidized corn starches varying in amylose content. *Carbohydrate Research* **2006,** 341, (11), 1896-1915.

Asociación Colombiana de Ingenieros de Petróleos – ACIPET
Carrera 14 No. 97-63, Piso 5
PBX: (601) 6411944 - www.acipet.com

48. Andreatta, G.; Bostrom, N.; Mullins, O. C., High-Q ultrasonic determination of the critical nanoaggregate concentration of asphaltenes and the critical micelle concentration of standard surfactants. *Langmuir* **2005,** 21, (7), 2728-2736.

49. Medina Erao, O. E.; Gallego, J.; Olmos, C. M.; Chen, X.; Cortés, F. B.; Franco, C. A., Effect of Multifunctional Nanocatalysts on n-C7 Asphaltene Adsorption and Subsequent Oxidation under High Pressure Conditions. *Energy & Fuels* **2020**.
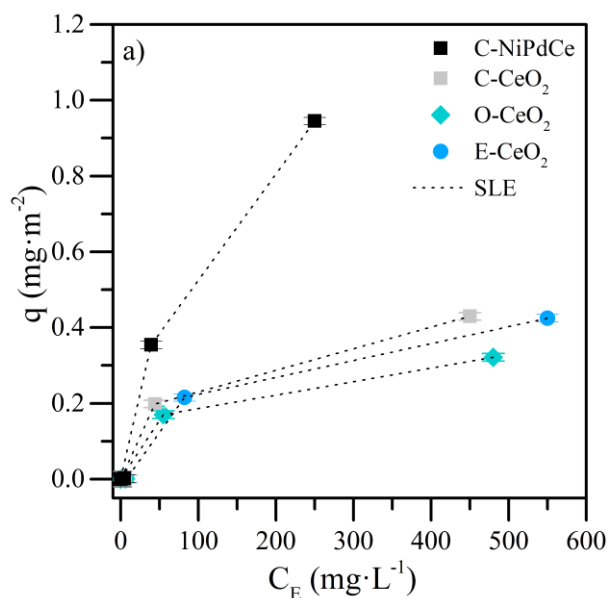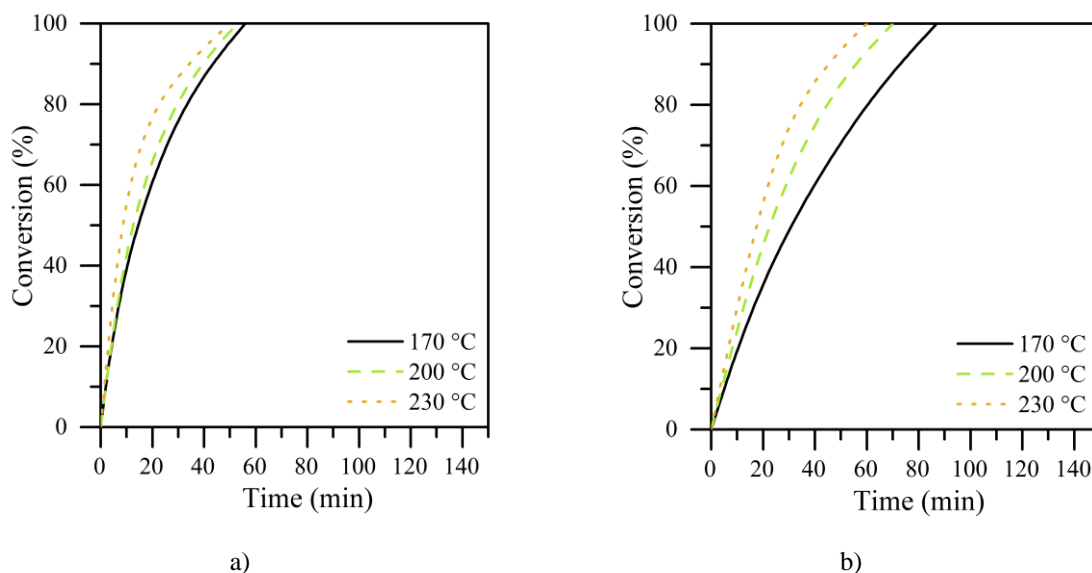
Appendix A.

Figure 1. experimental adsorption of *n*-C$_7$ asphaltene over CeO$_2$ nanoparticles with different morphologies (cubic, orthorhombic, and spherical), and cubic doped with Ni and Pd in a mass fraction of 1 % (dotted lines represent the SLE fitting).
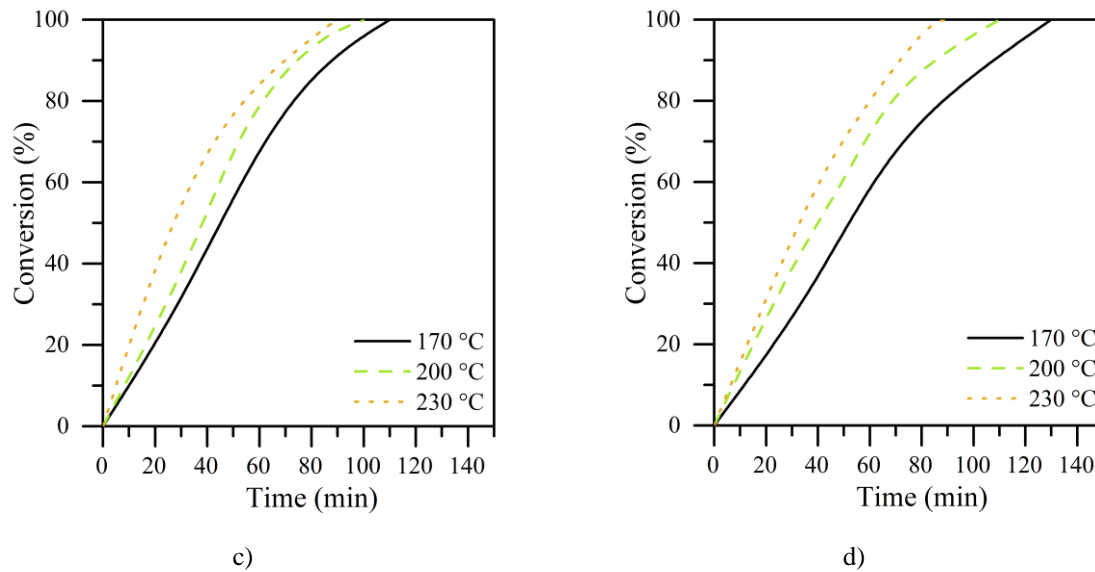
c)   d)

Figure 2. Isothermal conversion of n-C_7 asphaltenes steam gasification adsorbed on a) C-NiPdCe, b) C-CeO$_2$, c) O-CeO$_2$, d) S-CeO$_2$. Nitrogen flow: 100 ml·min^{-1}, steam flow: 6.7 ml·min^{-1}, and sample mass 5 mg.

Asociación Colombiana de Ingenieros de Petróleos – ACIPET
Carrera 14 No. 97-63, Piso 5
PBX: (601) 6411944 - www.acipet.com